Multiphysics Simulation for the Optimization of an Optoelectronic-Based Tactile Sensor

Gianluca Laudante[a], Olga Pennacchio and Salvatore Pirozzi[b]

Università degli Studi della Campania "Luigi Vanvitelli", Dipartimento di Ingegneria, Aversa (CE), Italy

Keywords: Tactile Sensor, Multiphysics Simulation, Optics, Mechatronics.

Abstract: Robotic systems are more and more present in various contexts such as industrial, domestic, logistic, health-care, and others. For this reason, robots are being used for increasingly complex tasks which require skills like dexterity and precision. These capabilities are achieved by means of sensory systems that give that robot the perception of the environment. Sensors, before being produced and distributed, need to be suitably designed in order to fulfil the specifics that a task requires. During the design process, simulation methods are really important to analyze the characteristics of a designed product before actually producing it, so as to avoid waste of time and money. This paper aims at proposing a method for simulating a tactile sensor based on optoelectronic technology considering both the optical and mechanical interfaces, as well as their coupling. Also, it exploits both simulation and experiment results in order to discuss the best choice for the shape to use for the realization of reflective cells.

1 INTRODUCTION

Nowadays, robotics systems are increasingly used to carry out complex tasks in cluttered environments, where abilities such as dexterity and precision are essential. To provide the robots with the necessary capabilities, sensory systems are required. These are mainly cameras, useful for having an overall view of the working scene, proximity and distance sensors, for avoiding collisions with the environment, and tactile sensors, which allow estimating the physical and geometrical properties of the manipulated objects, information of paramount importance for the execution of robotic grasping and manipulation tasks.

Tactile sensing, in particular, is receiving a lot of interest in the last few years since it can bring new possibilities for automating processes, currently carried out by human workers, in several fields such as logistics, people assistance, prosthetics, manufacturing, automotive and aerospace industry. Thanks to the growing interest, many new tactile sensors based on different technologies are being developed. For example, the Gelsight (Wang et al., 2021) and Tac-Tip (Ward-Cherrier et al., 2018) sensors use high-resolution RGB cameras to detect the deformation of a deformable mechanical interface, the Contactile sensor (Khamis et al., 2019) exploits optoelectronic

components to retrieve information about the contact, while the GTac sensor (Lu et al., 2022), inspired by the human sense of touch, integrates both piezoresistive and Hall sensors in a multilayered structure. Despite the technological progress and the development of these new sensors, the research in the analysis and design of tactile sensors remains an open field with many investigated problems. Since all the aforementioned sensors present the combination of at least two parts, i.e., an external mechanical interface and an internal, usually electronic, component to transduce deformations in a different signal depending on the used technology, multiphysics modelling and simulation are of paramount importance for improving and optimizing the design and analysis processes.

To the best of the authors' knowledge, in literature, there is a lack of methods for simulating both the layers composing the tactile sensors, especially for those based on optical technology like the one considered in this work, and their coupling. In fact, authors in (Amiri et al., 2022) simulate a GaN-based integrated LED-photodetector system using only the optical physics, in (Alqurashi et al., 2022) the optical part of a low concentrator photovoltaic system is simulated, (Ferreira et al., 2022) studies the vertical p-n junction photodiodes according to CMOS technology through the optical-semiconductor interfaces, while authors in (Cirillo et al., 2014) consider a FE analysis of a silicone deformable interface using mechanical physics. However, all these works do not take into ac-

---

[a] https://orcid.org/0000-0003-4009-8287
[b] https://orcid.org/0000-0002-1237-0389

count the coupling of the mechanical and the optical interfaces. Indeed, the main objective of this paper is the development of a simulation model for the design and optimization of optic-based tactile sensors, considering the coupling of the optoelectronic layer and the mechanical deformable layer.

The rest of the paper is structured as follows: Section 2 reports the procedure used to refine the optoelectronic component parameters in order to obtain a detailed optical model, also by means of comparison between simulated data and the datasheet provided by the manufacturer. This section also presents the mechanical model of the deformable layer, and the results of the coupling of the validated optical model and the mechanical model to optimize the shapes of the reflective cells on the basis of the sensor sensitivity. Section 3 reports some experimental tests using a real sensor whose results are compared with the ones from the simulations and among the different shapes of the reflective cells, and, finally, section 4 provides the conclusions and some possibilities for future advancements.

2 SIMULATION MODEL

The tactile sensor considered for this paper, reported in detail in (Cirillo et al., 2021), is constituted by a matrix of taxels, in which each taxel is based on the use of a LED-phototransistor couple (integrated within a single photo-reflector), and a deformable layer positioned above the components.
This section describes how the models of the optoelectronic component and the mechanical deformable layer have been realized for the simulation of the complete sensor, and reports the results obtained by the simulation of the coupled model.

2.1 Optical Model

The following reports the analysis of the optoelectronic device's geometry, necessary to reproduce adequately the optical component model in *COMSOL Multiphysics* with the *Ray Optics Module*, and the performance of the obtained model.

2.1.1 Component Analysis

The core component of the tactile sensor is the NJL5908AR photo-reflector, currently manufactured by Nisshinbo Micro Devices and it integrates into the same case an infrared Light Emitting Diode (LED), with the peak wavelength @925 nm and an optically matched phototransistor. The dimensions of the com-

ponent are $1.06 \times 1.46 \times 0.5$ mm, as reported in the datasheet (NJL5908AR Datasheet, 2015). Instead, the dimensions of the LED emitting surface and phototransistor receiving area have been estimated by means of a high-resolution image (see Fig. 1), acquired with an optical microscope (Model Dino-Lite AM413T).
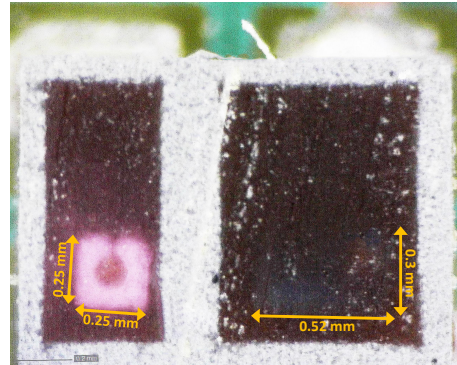

Figure 1: Dimensions of LED emitting surface and phototransistor receiving area.

The phototransistor has a rectangular receiving area equal to 0.52×0.3 mm, while the external square emitting area of the LED has a side equal to 0.25 mm. The central part of the LED does not emit rays, as visible from Fig. 1, and it is suitably modelled as it appears. The test conditions of the photo-reflector consider the output current when the infrared signal from LED is reflected by an aluminium surface, positioned in front of the component. As reported in the photo-reflector datasheet, the current in the phototransistor changes when the distance z between the component and the reflective surface varies from 0 mm to 2.5 mm. The characteristic is non-monotonic, and in particular, it increases if z varies from 0 mm to 300 μm, while it decreases if z exceeds 300 μm. Besides, the current follows a different trend when z is maintained equal to 0.7 mm and the aluminium plate is separately moved on this fixed plane along two orthogonal directions, named x and y, until the space among the reflective plane and the photo-reflector edges varies from 0 mm to 1.5 mm. In order to allow the evaluation of optical model quality presented in the following, by means of a comparison of simulated data with the ones from the datasheet, the main relations exploited in the multiphysics simulator are here recalled. By defining with I_{ph} the output current from the receiver and with P_o the optical power incident on it, its responsivity can be defined as $R = \frac{I_{ph}}{P_o}$. The Quantum Efficiency (Q.E.), which considers the relation among the incident photons and electron-hole pairs that are responsible for the photo-current, can be defined as $\eta = \frac{I_{ph}}{e_c} / \frac{P_o}{h\nu}$, where ν is the frequency of the

optical wave, e_c is the constant value of the electron charge and h is the Planck's constant. By combining the previous equations, it results that the responsivity depends on the wavelength: $R = \eta \frac{e_c}{h\nu} = \eta \frac{e_c \lambda}{hc}$, where the constant c is the speed of light. Thus, when the wavelength λ is fixed, the responsivity R is constant. As a consequence, the current I_{ph} and the power P_o are proportional, and the normalized current values reported in the datasheet can be directly compared with the normalized power values computed in the simulation multiphysics environment, in order to evaluate the accuracy of the optical component model.

2.1.2 Geometrical Optics

The *Ray Optics Module* exploits the *Geometrical Optics* theory for the component modelling. The ray trajectory is computed by solving the following six coupled first-order differential equations for the **k** and **q** components

$$\frac{d\mathbf{q}}{dt} = \frac{\partial \omega}{\partial \mathbf{k}} \qquad \frac{d\mathbf{k}}{dt} = -\frac{\partial \omega}{\partial \mathbf{q}} \qquad (1)$$

where **k** is the wave vector, **q** is the position vector, ω is the angular frequency and t is the time.

Concerning the initial generation of rays from the emitter surface, they are released by using the *release from boundary* option. In detail, the ray release positions are related to a *projected plane grid* constituted by a *Number of points per release* equal to N. Hence, the ray initial direction can be specified, in different modalities, by assigning values to the degrees of freedom corresponding to the wave vector **k** of each ray. For the chosen *Conical* option the initial wave vector is sampled from a distribution in the wave vector space at each release point. The *Number of rays in wave vector space* is equal to N_w. In 3D the initial wave vector components (k_x, k_y, k_z) are sampled according to the expressions

$$k_x = \frac{\omega n}{c} \sin\theta \cos\varphi \qquad (2)$$

$$k_y = \frac{\omega n}{c} \sin\theta \sin\varphi \qquad (3)$$

$$k_z = \frac{\omega n}{c} \cos\theta \qquad (4)$$

where

- φ is the azimuthal angle and it is uniformly distributed in $[0, 2\pi]$,
- θ is the polar angle and it can vary in $[0, \gamma]$, with γ the *cone angle* measured with respect to the vertical z axis, orthogonal to the optical component,
- n is the refractive index of the material.

2.1.3 Photo-Reflector Model

The model of the optical component is built in *COMSOL Multiphysics* by using the *Ray Optics Module* options described above, and the time-dependent study *Ray Tracing* is used to solve the differential equations in order to compute the ray trajectories. First of all, in order to model the emitter, the *release from boundary* option has been applied to the LED emitting surface as experimentally measured from Fig. 1, with a *projected plane grid* with $N = 20$ points and $N_w = 3000$ rays released from each point (see Fig. 2). The *cone angle* γ, initially fixed equal to $90°$, during the model refinement has been selected equal to $88°$, by means of a trial and error procedure.
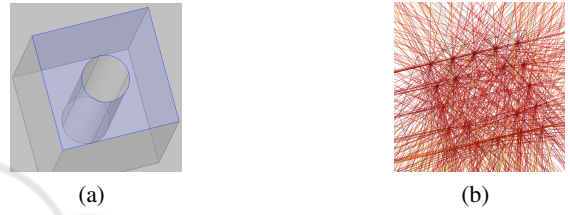

Figure 2: LED model: (a) boundary selected as emitting surface, and (b) projected plane grid with released rays.

Then, the aluminium plate is modelled as a rigid plane with the bottom surface completely reflective, by using the *mirror* option with the absorption coefficient $\alpha = 0$. Instead, for the phototransistor, the *wall* option is required to fix the ray position and the wave vector at the instant its surface is struck by a ray. At last, the *ray detector* option is used to compute the desired quantities related to the rays that struck the receiving area of the phototransistor. In particular, the interesting variables are the total number of the rays N_{sel} in the selected area and the total optical power P_o transmitted to the detector. Figure 3 shows an example of ray trajectories available during a simulation.

In order to simulate the optical component model and compare the simulation data with the datasheet, the described model has been solved by varying the distance along the $z-$axis between the optical compo-
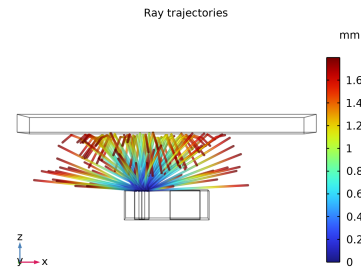

Figure 3: Ray trajectories with the reflective surface at a distance $z = 1.5$ mm, and at the instant time $t = 6e - 12$ s.

nent and the reflective surface from 0 mm to 2.5 mm with a step of 0.02 mm, by using a *parametric sweep* option. For each step, the optical power P_o has been computed and at the end of the sweeping phase the P_o data have been normalized with respect to the maximum value and compared with the normalized photocurrent reported in the datasheet, according to the observation detailed in Sec. 2.1.1. Figure 4 reports the comparison between reference data and simulation data. In order to completely verify the optical
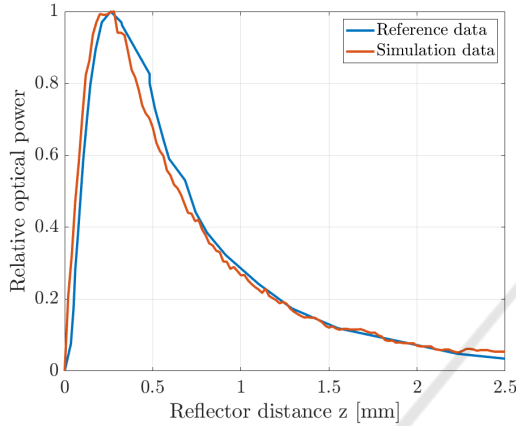
Figure 4: Optical power along $z-$axis: comparison of reference data and simulation data.

component model, also the features corresponding to the aluminium plate movements along x and y axes have been simulated and compared with the datasheet. Figures 5 and 6 show the optical power with respect to the reflective surface edge distance. From the figures it is evident that the model well reproduces the component features along the x and z axis, while along the y axis the reconstruction is qualitatively lower. However, for the following analysis, the fundamental relation is only the one along z axis.
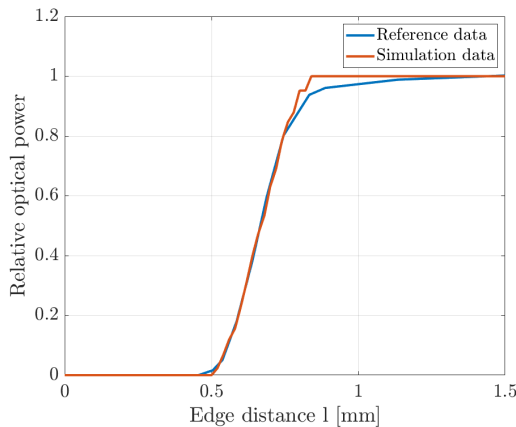
2.2 Mechanical Model

In the following, the module exploited for the realization of the model for the deformable layer of the sensor is briefly presented, and the geometry of the realized mechanical structure is detailed.

2.2.1 Structural Mechanics Module

The *Structural Mechanics Module* solves the motion equations with a constitutive model for the solid material and it computes as results mechanical variables (e.g., displacements, strain, etc.). It also allows the reproduction of geometric nonlinearities, contact conditions and loads. The analysis of the finite deformations is based on the total Lagrangian formulation, in which the computed state is referred to the material configuration rather than to the current position in the space. It can be formalized as $\mathbf{x} = \mathbf{X} + \mathbf{u}(\mathbf{X}, t)$, where $\mathbf{x}$ are the spatial coordinates, $\mathbf{X}$ are the material coordinates and $\mathbf{u}$ are the displacements. A boundary load can be defined by specifying the application area A, and the force components $\mathbf{F}_{tot} = (f_x, f_y, f_z)$ or the force per unit area $\mathbf{F}_A = \mathbf{F}_{tot}/A$.

2.2.2 Deformable Layer Model

The geometry of the mechanical structure is composed of 9 taxels, organized in a 3×3 matrix, and numbered as reported in Fig. 7. The photo-reflector is optically centered with respect to the taxel mechanical geometry: the optical center is the mean point between the center of the LED and the center of the phototransistor and it is aligned with the geometrical center of the taxel structure. The deformable pad is the hollow block obtained by removing the array of nine smaller blocks with a spatial resolution of 3.55 mm.

The hallow parts have different shapes, as shown in Fig. 8. In the parallelepiped geometry, every sin-
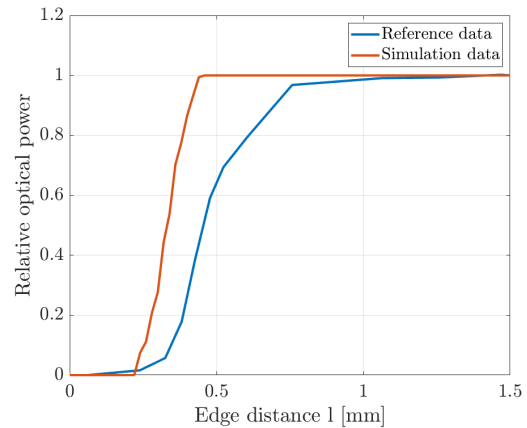

Figure 5: Optical power along $x-$axis: comparison of reference data and simulation data.

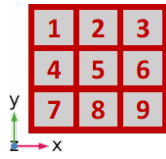Figure 6: Optical power along $y-$axis: comparison of reference data and simulation data.

Figure 7: Taxel numbering used in the simulations.

gle cell has dimensions $2.55 \times 2.55 \times 1.55$ mm and the distance between the optical component and the reflective surface is 1.05 mm, by taking into account that the component has a height of 0.5 mm. The cylindrical taxel is obtained from the parallelepiped case by using as a base the circle inscribed in the parallelepiped base, with radius $r = 1.275$ mm, and the same height equal to 1.55 mm. Analogously, the hemispheric cell has radius $r = 1.275$ mm and r also represents the distance between the emitting surface of the optical component and the top of the dome. The intermediate case is the spherical shape of radius R double with respect to the cylinder case, i.e. $R = 2r$. With the equation $h_s = R - \sqrt{R^2 - r^2}$, it is possible to compute the height of the spherical section, that is 0.342 mm. By fixing the distance between the photo-reflector emitting surface and the top of the dome in this case equal to 1.1 mm, the cylinder on which the spherical section is built has a height of 1.258 mm. The external dimensions of the whole pad are $11.65 \times 11.65 \times 4.55$ mm.

The material of the pad is selected from the available library as silicone with Young's modulus equal to 4.16 MPa, which falls into Scale A durometer hardness. From an optical point of view, the lateral walls of taxels are modelled as totally absorbent (i.e., $\alpha = 1$), while the above surfaces are simulated as completely reflective (i.e., $\alpha = 0$) with isotropic scattering
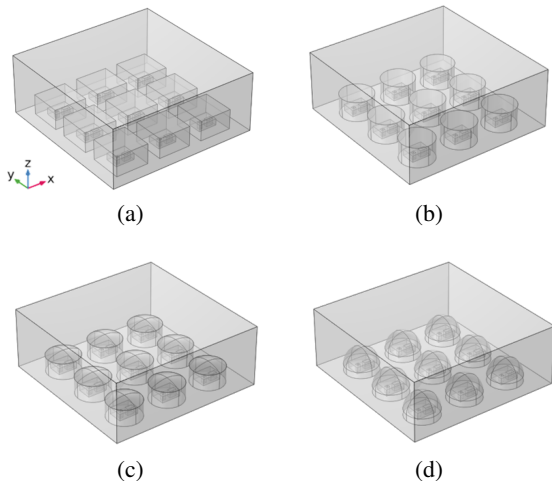

Figure 8: Tested shapes: (a) parallelepipeds, (b) cylinders, (c) spherical sections, and (d) hemispheres matrix.

condition. Regarding the mechanics, a variable total force on the top surface of the whole pad is applied and a fixed constraint is defined for the bottom of the pad (i.e., $\mathbf{u} = 0$ in all directions).

2.3 Coupled Model Results

The multiphysics coupling is realized by performing the *Ray Tracing* analysis after the computation of the structural deformation. In detail, the final solutions are obtained by means of a two-step analysis, repeated with incremental values of applied external forces. The first step solves only the solid mechanics physics, including the geometric nonlinearities, while the second ray tracing step solves geometrical optics physics, including the geometric nonlinearities in order to take into account the deformed geometry, obtained from the first step. The external forces have been incrementally applied to the deformable pad by means of a parametric sweep option. By applying separate and coupled force components, different analyses have been carried out to evaluate taxel features. For each considered taxel geometry, the optical power P_o has been computed with respect to force values in order to quantify and compare the considered features. The first analysis has been carried out by applying to the pad only a vertical force f_z, with values from 0 N to -20 N with a step of 0.5 N. Figure 9 reports the optical powers on the phototransistor surfaces with respect to the force values in the parallelepiped case. For the other geometries the same data have been acquired, and the sensitivity with respect to f_z has been evaluated as the maximum slope of all curves, for all considered shapes. The following maximum sensitivity values have been obtained: $1.48e-4$ W/N for the parallelepiped geometry, $1.11e-4$ W/N in the cylindrical case, $1.4e-4$ W/N for the spherical shape, $2.48e-4$ W/N in the hemispheric geometry. The second type of analysis has been carried out to evaluate the sensitivity with respect to tangential force components. To this aim, a constant normal force equal to -8 N is applied on the boundary, and at the same time variable tangential force components have been applied from 0 N to a maximum value, depending on the simulation convergence with respect to the taxel geometry. In detail, the simulation is convergent with tangential components up to -11 N in the parallelepiped case, -13 N for the cylindrical and the hemispheric shapes, -8 N for the spheres matrix. Data similar to Fig. 9 can be considered in order to evaluate the sensitivity with respect to a tangential force applied along *x* or *y* directions. Obatined results are: $2.48e-4$ W/N for the parallelepiped geometry, $1.87e-4$ W/N in the cylindrical case, $2.66e-4$ W/N
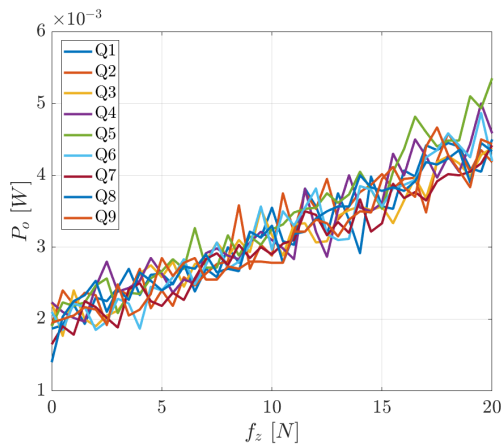
Figure 9: Optical powers with respect to the normal force in the parallelepiped case.

for the spherical shape, $3.91e-4$ W/N in the hemispheric geometry. Since the cylindrical case always presents the lowest sensitivity, it has not been considered for the experimental comparison in the following section. Figure 10 allows additional observations about sensitivity, by showing how the taxel matrix appears like a skew-symmetric matrix in terms of mechanical displacement and optical power for some simulation instants in presence of a tangential force applied along the pad secondary diagonal. It is evident how the taxels 3 and 7 present the greater difference in values, the taxels 4 and 8 with respect to taxels 2 and 6 present a medium difference and the taxels on the main diagonal are almost similar. This demonstrates the relations among the force components, the mechanical displacements and the optical power measured by photo-transistors. The matrix symmetry is strictly related to force directions.

3 EXPERIMENTAL EVALUATIONS

By considering the complexity of the deformable pad both in terms of mechanical and optical features, also an experimental evaluation of taxel performance has been carried out. A suitable setup has been prepared to evaluate some properties for the taxel: linearity, sensitivity, hysteresis and repeatability. Linearity and sensitivity are of paramount importance in sensor characterization, but also hysteresis and repeatability are computed. To obtain a complete sensor characterization, in this section experiments by applying only normal forces and both normal and tangential components have been considered. The setup is shown in Fig. 11 and its main components are: a *Robotous*
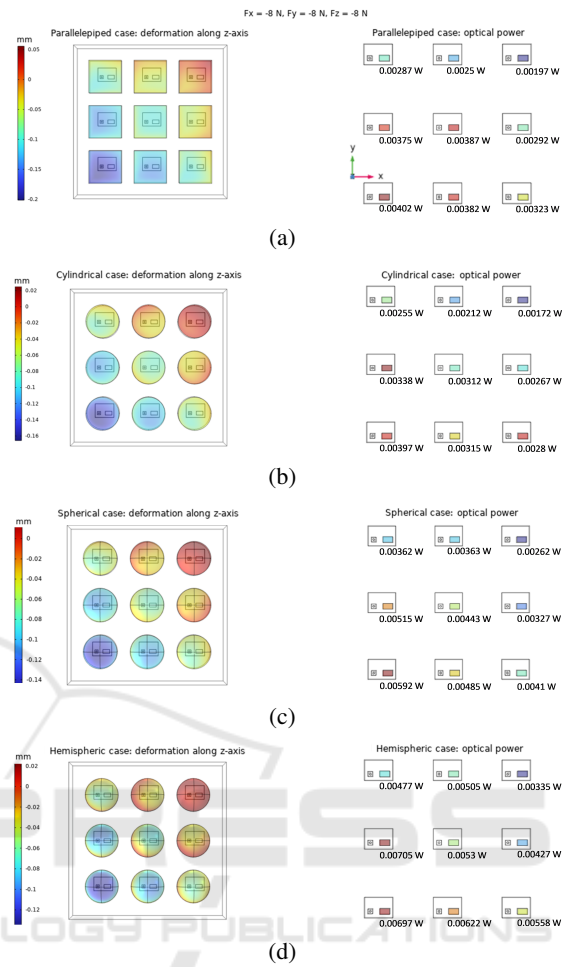

Figure 10: Deformations along $z-$axis (left) and optical powers (right), with a tangential force equal to -8 N along the secondary diagonal of taxel matrix: (a) parallelepiped case, (b) cylindrical case, (c) spherical case, (d) hemispheric case.

RFT40-SA01-D $6-$axes force/torque sensor (used as reference sensor), a 6×2 tactile sensor (equipped with 3 pads with different taxel geometries) and an UR5e robot manipulator (to apply external loads).
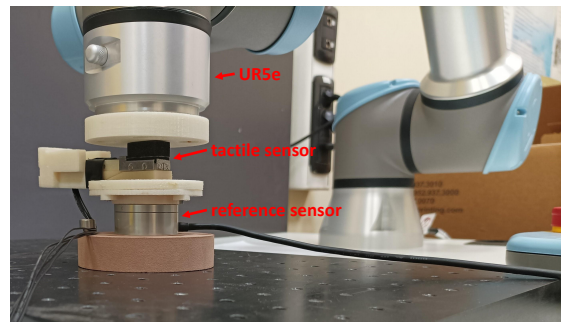

Figure 11: Experimental setup.

For the experiments, a sensor with a matrix 6×2 has been used since the printed circuit board with optical components was already available in the laboratory (see Fig. 12 for taxel numbering). This choice does not limit the analysis in terms of linearity, sensitivity, hysteresis and repeatability.
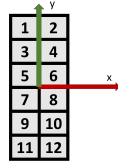

Figure 12: Taxel numbering used in the experiments.

The UR5e cobot is directly programmed by using its Graphical User Interface (GUI) available from the teach pendant. It is used to apply the same force components on the 3 different pads prepared with the 3 different taxel shapes selected on the basis of simulations (e.g., parallelepiped, spherical and hemispheric). Figure 13 reports pictures of deformable pads realized with silicone molding technique and used in the experiments.

3.1 Sensor Characterization

As for simulations, two kinds of experiments have been carried out in order to compare the tactile sensor characteristics with respect to taxel shapes: the first by applying only normal force in order to evaluate the sensor along the z axis and the second by applying also tangential components for the evaluation along the x and y axes. In the first experiment, the robot is initially positioned almost in contact with the pad, and then it is vertically moved of $1.1\,\text{mm}$ along z axis in $50\,\text{s}$ (by resulting a velocity of $0.022\,\text{mm/s}$) in order to apply a normal force to the pad. During the linear movement in the operative space the robot applies a normal force from $0\,\text{N}$ to $10\,\text{N}$ with a velocity of $0.2\,\text{N/s}$. Figure 14 reports the normal force f_z signal from the reference sensor and the taxel voltage variations Δv_i acquired during the experiment for the parallelepiped case. From these data the sensitivity
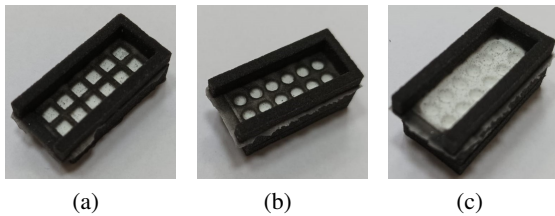

(a)   (b)   (c)

Figure 13: Pad with different taxel geometries: parallelepiped case (a), spherical case (b), and hemispheric case (c).

for each taxel can be evaluated as the mean slope of the force-voltage relation. It appears different for the 12 taxels, by varying from a minimum of $0.0196\,\text{V/N}$ achieved by the taxel 3 to a maximum of $0.0355\,\text{V/N}$ reached by the taxel 11. The taxel with maximum sensitivity has been used to evaluate the other features, since it corresponds to the worst case. In particular, the hysteresis error has been evaluated as

$$e_h = \frac{|\Delta v_{incr} - \Delta v_{decr}|}{v_{max}} \cdot 100 \qquad (5)$$

where Δv_{incr} and Δv_{decr} are the voltage variations corresponding to two consecutive time ranges when the force, in Fig. 14, increases and decreases respectively, while v_{max} is the maximum Δv_i value reached during the experiment. Similarly, the repeatability error has been evaluated as

$$e_r = \frac{|\Delta v_a - \Delta v_b|}{v_{max}} \cdot 100 \qquad (6)$$

where Δv_a and Δv_b are the voltage variations corresponding to the two time ranges when the force, in Fig. 14, increases (or decreases). For the parallelepiped case the hysteresis error is $e_h = 1.88\%$ and the repeatability error is $e_r = 2.08\%$ for the taxel 11. Figure 15 reports the graphs used for e_h and e_r computation. For the spherical geometry, the same acquired data are reported in Fig. 16. The minimum sensitivity is $0.00467\,\text{V/N}$, reached by the taxel 10, while the maximum one is $0.00716\,\text{V/N}$, achieved by the taxel 11. Figure 17 reports data of taxel 11 for hysteresis and repeatability, and the computed errors are $e_h = 6.87\%$ and $e_r = 1.33\%$, respectively. Finally, for the hemispheric shape the data are reported in Fig. 18. The sensitivity ranges from a minimum of $0.00335\,\text{V/N}$ for the taxel 1 to a maximum of $0.00869\,\text{V/N}$ for the taxel 8. As for previous case, Fig. 19 reports data related to the taxel with the maximum sensitivity (taxel 8 for this shape) in order to
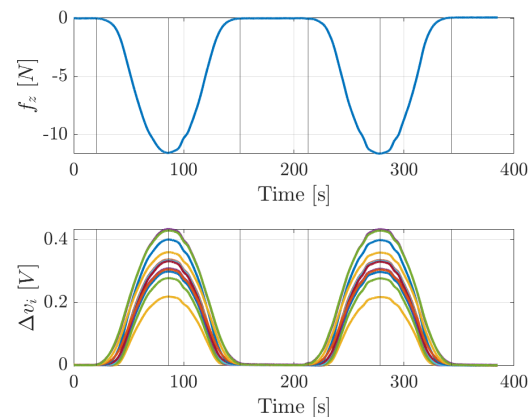

Figure 14: Parallelepiped case: (top) normal force applied and (bottom) taxel voltage variations.
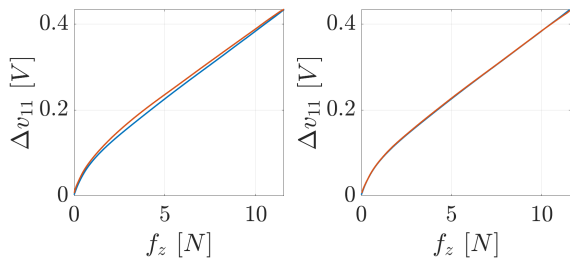
Figure 15: Parallelepiped case: (left) data for hysteresis error and (right) data for repeatability error.

evaluate the hysteresis error $e_h = 10.3\%$ and the repeatability error $e_r = 3.35\%$. The main important feature highlighted from these experimental data with respect to simulation data is the nonlinearity in the force-voltage relations. In particular, while the parallelepiped case is almost linear (see Fig. 15), the spherical case shows a non negligible nonlinearity (see Fig. 17) and the hemispheric case a high nonlinearity (see Fig. 19). By evaluating the nonlinearity error as

$$e_{nl} = \frac{|\Delta v_{incr} - \Delta v_{nom}|}{v_{max}} \cdot 100, \qquad (7)$$

where Δv_{incr} is the voltage variations corresponding to the first time range when the force increases, and Δv_{nom} is the voltage variations corresponding to ideal linear case, the following values are obtained: $e_{nl} = 3.18\%$ for the parallelepiped case, $e_{nl} = 5.38\%$ for the spherical case, and $e_{nl} = 11.7\%$ for the hemispheric one. Thus, the performance in terms of linearity are clearly better for the parallelepiped case.

The comparison of characteristics along the x and the y axes also has been carried out. In order to reproduce simulated case, the robot, initially positioned almost in contact with the pad, is vertically moved of 1.1 mm along z axis in 50 s, by reaching a constant normal force of about 10 N. Then, the robot is moved of 1 mm along x−axis and 1 mm along y−axis simul-
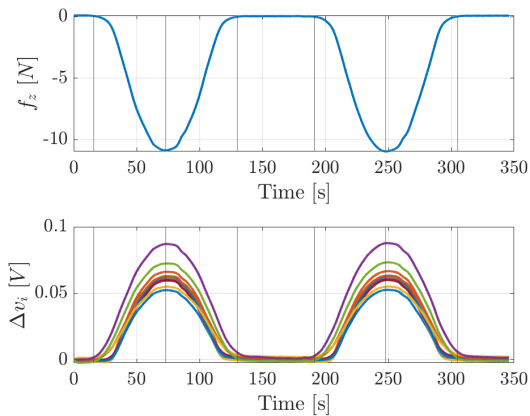

Figure 16: Spherical case: (top) normal force applied and (bottom) taxel voltage variations.
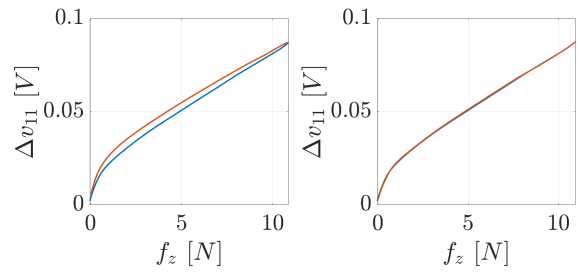

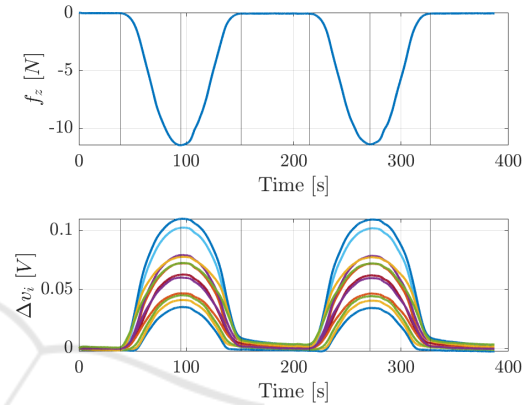Figure 17: Spherical case: (left) data for hysteresis error and (right) data for repeatability error.

Figure 18: Hemispheric case: (top) normal force applied and (bottom) taxel voltage variations.

taneously, by obtaining a diagonal tangential force. Also in this case the velocity is 0.022 mm/s and the trajectory is executed forward and backward, in order to obtain an increasing and decreasing phase for the tangential force. The sensitivity with respect to tangential force components have been evaluated on the same taxels selected from the normal case (i.e., the ones with the maximum sensitivity with respect to normal force). For the parallelepiped case, the taxel 11 presents a sensitivity along the x−axis equal to 0.0342 V/N and along the y−axis equal to 0.0314 V/N (see Fig. 20). For the spherical geometry, the taxel 11 reaches a sensitivity of 0.00271 V/N along the x−axis and 0.00276 V/N along the y−axis (see Fig. 21). At last, for the hemispheric case the taxel 8 presents a sensitivity of 0.00668 V/N along the x−axis and of 0.00569 V/N along the y−axis (see Fig. 22).
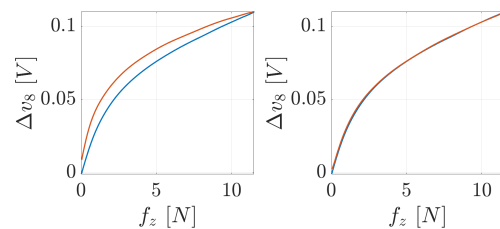

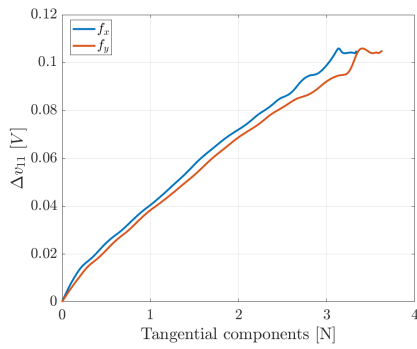Figure 19: Hemispheric case: (left) data for hysteresis error and (right) data for repeatability error.

Figure 20: Parallelepiped case: voltage variations with respect to tangential force components.

3.2 Comparison and Discussion

In order to compare simulation and experimental data among the different shapes for the reflective cells, the main important data have been summarized and discussed in this section. First of all, the sensitivity with respect to both normal and tangential components (see Tab. 1), estimated from simulation data, show that the cylindrical shape presents the lower values (particularly for the tangential case) and hence the experimental case has not been implemented to reduce the case studies. Among the other cases the sensitivity is almost of the same order. Obviously, in simulation all taxels of the same shape present the same features. Instead, by considering the experimental data, the taxel responses are different due to realization processes of electronic and mechanical components, hence it could be interesting to evaluate the minimum and maximum sensitivities. Table 2 summarizes these sensitivities for the different shapes. The absolute values cannot be directly compared with simulated results, since the units are different, but both cases (minimum and maximum) show similar sensitivity for spherical and hemispherical cases, while parallelepiped case is more sensitive up to one order of magnitude. This difference with
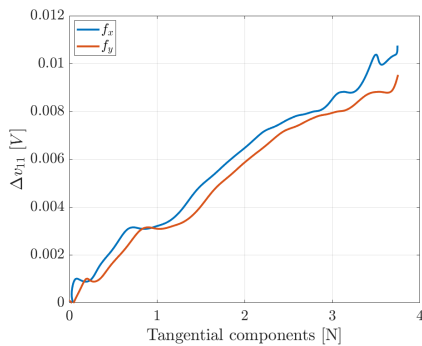

Figure 21: Spherical case: voltage variations with respect to tangential force components.
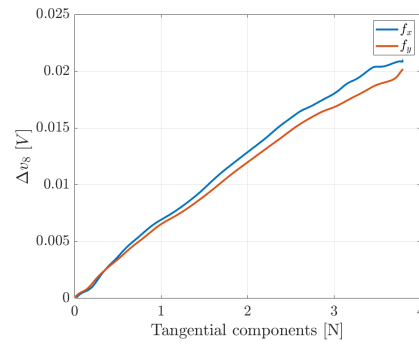
simulation case probably depends on the mechanical realization trough silicone moulds technique of pads by means of 3D printed moulds: the flat surface (in parallelepiped case) can be perfectly realized, while the spherical and hemispherical shapes are locally approximated with small discrete steps by the 3D print technology. The sensitivities experimentally evaluated with respect to tangential components, and reported in Tab. 3, confirm the same observations done for normal force: the parallelepiped case shows a sensitivity higher of one order of magnitude. Finally, the main feature highlighted from the experiments is the nonlinearity shown by the different shapes. As summarized in Tab. 4, the spherical case presents a nonlinearity almost double with respect to the parallelepiped case and the hemispheric case almost four times more. As a consequence the parallelepiped case appears as the best choice by considering its features also with respect to current manufacturing processes.

Table 1: Simulations: sensitivity to normal and tangential forces with respect to taxel shapes.

	Normal[W/N]	Tangential[W/N]
Parallelepiped	1.48e-4	2.48e-4
Cylindrical	1.11e-4	1.87e-4
Spherical	1.4e-4	2.66e-4
Hemispheric	2.48e-4	3.91e-4

Table 2: Experiments: minimum and maximum sensitivity to normal force with respect to taxel shapes.

	Min [V/N]	Max [V/N]
Parallelepiped	0.0196	0.0355
Spherical	0.00467	0.00716
Hemispheric	0.00335	0.00869

4 CONCLUSIONS

This paper reported the steps followed for the realization of the models of the two main parts compos-

Table 3: Experiments: sensitivity to tangential force with respect to taxel shapes.

	along x [V/N]	along y [V/N]
Parallelepiped	0.0342	0.0314
Spherical	0.00271	0.00276
Hemispheric	0.00668	0.00569

Table 4: Experiments: nonlinearity with respect to taxel shapes.

	Nonlinearity e_{nl} [%]
Parallelepiped	3.18
Spherical	5.38
Hemispheric	11.7

ing the considered optoelectronic-based tactile sensor: the photoreflector and the deformable layer. The simulation has been used to determine how different shapes of the reflective cells influence the performance of the sensor. In particular, four different shapes have been considered: parallelepiped, cylindrical, spherical, and hemispheric. Some tests have been carried out to check the response of the simulated model to different stimuli. Then, similar tests have been repeated in a real setup in order to compare the evaluated taxel shapes. Data from both the simulation results and the measurements from the real sensor have been used to discuss the best choice for the taxel shape, also by considering the limitations due to manufacturing processes. The results for properties such as linearity and sensitivity show differences between simulations and experiments probably due to the following reasons: in the simulation, the considered walls are completely reflective or absorbent, while the real pads have white and black walls that are not totally reflective or absorbent; the molds used for realizing the silicone pads, being 3D printed, present imperfections (i.e., grooves, small steps) that make the actual walls not smooth, differently from those in the simulation model, particularly for hemispheric and spherical cases. The consequence of this lack of smoothness is that, in the real case, the ray reflections are locally quite different from the simulated case.

Future studies will be devoted to enhancing the simulation model by taking into account the aforementioned imperfections, e.g., by modifying the mechanical model of the deformable layer taking into account the non-smooth surfaces due to the production process, or by investigating the possibility to consider different reflection modalities in the ray tracing technique.

REFERENCES

Alqurashi, M. M., Ganash, E. A., and Altuwirqi, R. M. (2022). Simulation of a low concentrator photovoltaic system using comsol. *Applied Sciences*, 12(7).

Amiri, P., Casals, O., Maur, M. A. d., and Prades, J. (2022). Ray tracing simulation of a gan-based integrated led-photodetector system. In *2022 Int. Conf. on Numerical Simulation of Optoelectronic Devices (NUSOD)*.

Cirillo, A., Cirillo, P., De Maria, G., Natale, C., and Pirozzi, S. (2014). A FE analysis of a silicone deformable interface for distributed force sensors. *AIP Conference Proceedings*, 1599(1):485–488.

Cirillo, A., Costanzo, M., Laudante, G., and Pirozzi, S. (2021). Tactile sensors for parallel grippers: Design and characterization. *Sensors*, 21(5).

Ferreira, G. M., Silva, V., Minas, G., and Catarino, S. O. (2022). Simulation study of vertical p-n junction photodiodes' optical performance according to cmos technology. *Applied Sciences*, 12(5).

Khamis, H., Xia, B., and Redmond, S. J. (2019). A novel optical 3d force and displacement sensor – towards instrumenting the papillarray tactile sensor. *Sensors and Actuators A: Physical*, 291:174–187.

Lu, Z., Gao, X., and Yu, H. (2022). Gtac: A biomimetic tactile sensor with skin-like heterogeneous force feedback for robots. *IEEE Sensors Journal*, 22(14):14491–14500.

NJL5908AR Datasheet (2015). *NJL5908AR Datasheet Ver.2015-02-17*. New Japan Radio Co. LTD, Tokyo, Japan.

Wang, S., She, Y., Romero, B., and Adelson, E. (2021). Gelsight wedge: Measuring high-resolution 3d contact geometry with a compact robot finger. In *2021 IEEE Int. Conf. on Robotics and Automation (ICRA)*.

Ward-Cherrier, B., Pestell, N., Cramphorn, L., Winstone, B., Giannaccini, M. E., Rossiter, J., and Lepora, N. F. (2018). The tactip family: Soft optical tactile sensors with 3d-printed biomimetic morphologies. *Soft Robotics*, 5(2):216–227.